Bimodality in zircon oxygen isotopes and implications for crustal melting on the early Earth

C.L. Kirkland [a,1,*], T.E. Johnson [a], J. Gillespie [a], L. Martin [b], K. Rankenburg [a,2], J. Kaempf [a], C. Clark [a]

[a] School of Earth and Planetary Sciences, Curtin University, Perth, WA 6845, Australia
[b] Centre for Microscopy, Characterisation and Analysis, The University of Western Australia, Perth, WA 6009, Australia

ARTICLE INFO

ABSTRACT

Zircons from the oldest dated felsic crust, the Acasta Gneiss Complex, Canada, provide key information that may help understand the generation of crust on our nascent planet. When screened to eliminate grains with secondary alteration by measuring relative hydration ($\Delta^{16}O^1H/^{16}O$), primary ≥ 3.99 Ga zircon cores show $\delta^{18}O$ of 5.88 ± 0.15 ‰, at the extreme upper (heavy) range for mantle values. Another early (≥ 3.96 Ga) zircon component indicates distinctly different, primary light $\delta^{18}O$ values ($\delta^{18}O \leq 4.5$ ‰). This bimodality in ancient zircon oxygen isotopes implies partial melting of both deep (lower crustal) and shallower (near surface) source rocks, responsible for felsic crust production on the early Earth. A similar bimodality in zircon $\delta^{18}O$ is recognised in data from other ancient cratons, albeit at different times. Although alternative (uniformitarian) interpretations may also satisfy the data, the tempo of this bimodality matches models of planetary high-energy impact flux, consistent with a fundamental role for bolide impacts in the formation of crustal nuclei on the early Earth.

1. Introduction

The primary (magmatic) oxygen isotopic composition in zircon crystals has provided important constraints on the conditions of partial melting on our early planet. Relative to Vienna Standard Mean Ocean Water (VSMOW), magmatic zircon crystals with Hadean (>4 Ga) and Archean (4.0–2.5 Ga) ages have primary $\delta^{18}O$ values that typically range from 3.0 ‰ to 8.0 ‰ (Valley et al., 2005). Zircon crystals in equilibrium with (and/or crystallising from) mantle-derived melts have $\delta^{18}O_{SMOW}$ values of 5.3 ‰ $\pm$ 0.6 ‰ (Mattey et al., 1994; Valley, 2003). However, incorporation of high $\delta^{18}O$ material, such as supracrustal rocks affected by relatively low-temperature (<200 °C) near-surface processes, increases the $\delta^{18}O$ composition of a magma and zircon grains crystallized therefrom. For example, granites derived from partial melting of, or that assimilated, metasedimentary rocks typically have bulk-rock $\delta^{18}O_{SMOW}$ values of 9–15 ‰ (O'Neil and Chappell, 1977) and contain magmatic zircon with $\delta^{18}O_{SMOW}$ in the range ~7–‰ (Valley, 2003). By contrast, magmatic rocks and zircons with sub-mantle $\delta^{18}O$ implies melting and/or assimilation of hydrothermally-altered rocks that interacted with

H₂O-rich fluids in the shallow crust (Bindeman et al., 2012; Smithies et al., 2015; Valley et al., 2005).

The Acasta Gneiss Complex (AGC) in the Northwest Territories, Canada (Supplementary Fig. S1), contains the oldest known evolved rocks on Earth, the tonalitic Idiwhaa gneiss, which contains zircon grains preserving U–Pb crystallization ages as old as c. 4.03 Ga (Bowring and Williams, 1999; Reimink et al., 2014, 2016; Stern and Bleeker, 1998). The oxygen isotopic composition of zircon in these gneisses provides clear evidence for the involvement of low-$\delta^{18}O$ hydrothermally-altered crust in the generation of their host magma. Given their similarities to modern-day 'icelandites', the Idiwhaa gneisses are considered by some to have formed through shallow-level fractionation of basaltic magma (Reimink et al., 2014). However, others have proposed an origin through shallow melting induced by a large meteorite impact (Johnson et al., 2018).

Here, we investigate oxygen isotopes in zircon from a sample (AC13) of the Idiwhaa gneiss, using secondary ionization mass spectrometry (SIMS). We compliment these data with laser ablation inductively coupled plasma mass spectrometry (LA–ICPMS) Lu–Hf isotope analysis

---

of garnet to better understand the effects of subsequent episodes of metamorphism. The results are compared to existing data from other ancient continental nuclei (cratons) and to models of impact flux, and provide insight into the processes of continental crust production on the early Earth.

2. Materials and methods

2.1. Sample

Sample AC13 comprises a peak assemblage of quartz (47 vol.%) + plagioclase (40 vol.%) + biotite (8 vol.%) + hornblende (4 vol.%) + garnet (1 vol.%), with accessory magnetite, ilmenite, apatite, and zircon. The rock consists of alternating quartzofeldspathic layers and garnet–hornblende-bearing bands with minor biotite that define the foliation. Garnet typically occurs as rounded or slightly elongate anhedral porphyroblasts (1–3 mm) that are partially replaced at their margins and along fractures by plagioclase and biotite with or without epidote (Supplementary Fig. S2). Rare inclusions of quartz, plagioclase, and hornblende in garnet show no clear preferred orientation.

Zircon grains from sample AC13 have been previously dated by SIMS (Kirkland et al., 2023). Based on cathodoluminescence (CL) images, their internal features were classified into three distinctive textural components (CL types 1–3) (Fig. 1). CL type 1 comprises highly-metamict cores containing areas of concordant zircon that yield an age of 3990 ± 2 Ma. CL type 2 consists of oscillatory zoned overgrowths on type 1 cores. CL type 3 forms homogeneous low-CL response rims that overgrow type 2 and which define an age of 3332 ± 12 Ma. Ion imaging of these zircon grains reveals that they preserve recrystallization fronts that penetrate inwards from the grain margins into the type 1 metamict cores, leaving a newly grown lower uranium content zone onto which new rim growth developed. Importantly, isolated isotopically undisturbed (e.g. concordant U–Pb) domains are preserved within the cores (Supplementary Data 1).

2.2. SIMS oxygen

Oxygen isotope ($^{18}O/^{16}O$) and $^{16}O^{1}H/^{16}O$ (OH^{-}) ratios were determined on previously-dated zircon grains from sample AC13 using a Cameca IMS 1280 at the Centre for Microscopy Characterisation and Analysis at the University of Western Australia (Supplementary Data 1) following the procedures of Kita et al. (2009). Samples were stored under heated vacuum for five days before analysis to limit in-chamber degassing and help minimise the background during analysis. A static ~2.7 nA Cs^{+} beam with an impact energy of 20 keV was focused to a 10 μm spot on the sample surface. A normal-incidence electron gun was used for charge compensation. Analyses used a magnification of 100x between the sample and field aperture, a 400 μm contrast aperture, a 3000 μm field aperture, a 90 μm entrance slit, 500 μm exit slits, and a 40 eV band bass for the energy slit with a 5 eV gap. Secondary O^{-} ions were
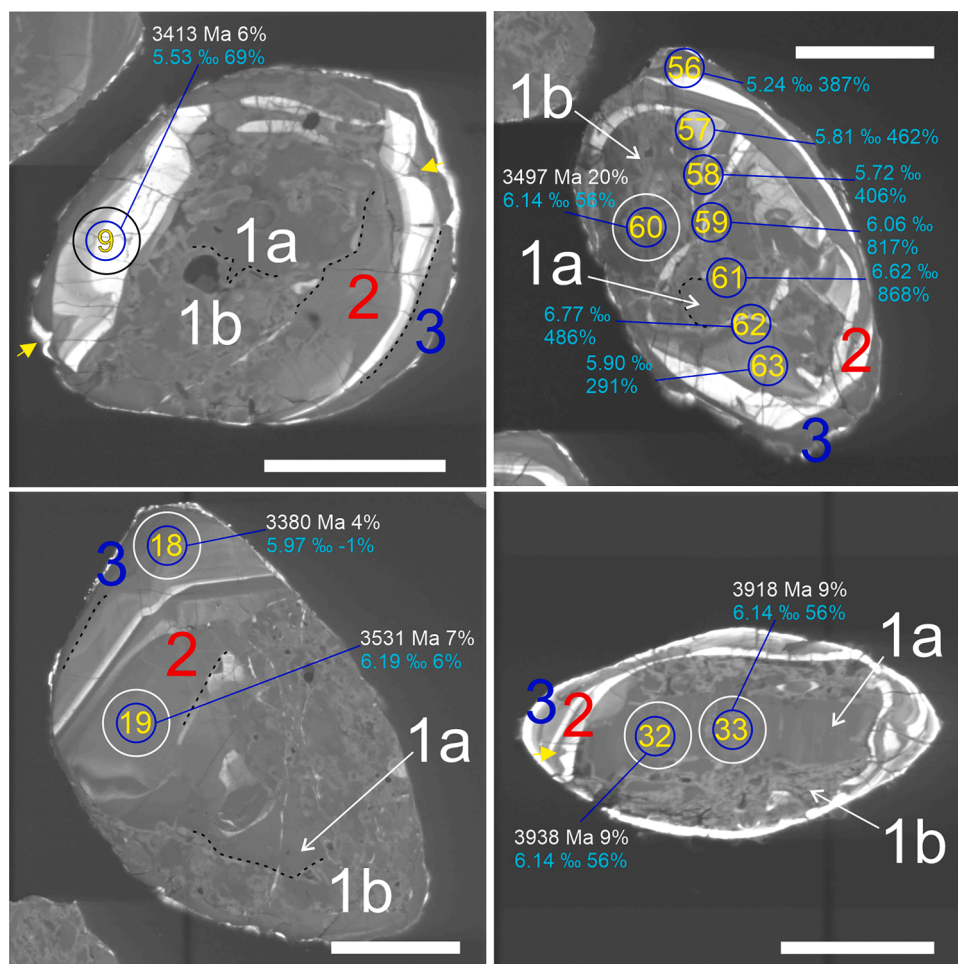

Fig. 1. Representative CL images of zircon crystals from sample AC13 Acasta Gneiss. U–Pb analysis spots are denoted by white ellipses (Kirkland et al., 2023). Oxygen analysis spots are denoted by blue ellipses. Numbers overlying the grain image indicate the CL types 1–3 (white, red, and blue font). $^{207}Pb/^{206}Pb$ ages and percent discordance are in white font; $\delta^{18}O$ in per mil and $\Delta^{16}O^{1}H/^{16}O$ in percent is in light blue font. Scale bars are 100 μm long. (For interpretation of the references to colour in this figure legend, the reader is referred to the web version of this article.)

accelerated to 10 keV and analysed with a mass resolving power of ~2400 using dual Faraday Cup detectors on the multi-collection axis. OH⁻ ions were collected using an on-axis, low background, Faraday cup fitted with 10^{11} Ω resistors operating at a mass resolving power of 7000. The $^{17}O^-$ and OH^- peaks are not completely resolved under these conditions, and the magnetic field was offset slightly to the high-mass side to avoid interference from $^{17}O^-$ on the OH^- peak. Spots were pre-sputtered for 30 s before automated peak centring in the field and contrast apertures. Uncertainty on isotopic ratios for individual analyses is calculated using the expressions given in the supplementary information of Kirkland et al. (2013).

Analyses consisted of 20 × 4 s cycles, which gave an average internal precision of 0.2 ‰ (2 SD mean). Bracketing of reference materials allowed for instrumental mass fractionation and drift corrections. The 91500 zircon (Wiedenbeck et al., 1995) was used as the primary oxygen isotope reference material and multiple grains of other reference zircon were run as unknowns. Using 91500 as the standard, the Plešovice zircon returned a weighted mean δ18O value of 7.97 ± 0.06 ‰ (95 % conf.; n = 21; MSWD = 2.4), consistent with the value reported by Liebmann et al. (2021); (δ18O of 7.94 ± 0.13 ‰). Analyses of the Mud Tank zircon indicated a δ18O value of 4.83 ± 0.07 ‰ (95 % conf.; n = 5; MSWD = 0.65), similar to the value reported by Valley (2003) (δ18O = 5.03 ± 0.20 ‰). Corrected $^{18}O/^{16}O$ ratios are reported in δ18O notation in per mil variations from VSMOW. A second oxygen session was performed on Grain X, during which analyses of the Mud Tank zircon indicated a δ18O value of 4.83 ± 0.26 ‰ (95 % conf.; n = 5; MSWD = 2.00). The stability of $^{16}O^1H/^{16}O$ measurements was monitored by measuring the $^{16}O^1H/^{16}O$ in the primary and secondary reference materials. The error reported for $^{16}O^1H/^{16}O$ for each single spot represents the internal error, as $^{16}O^1H/^{16}O$ is used qualitatively to assess whether the analysed domain was altered. Oxygen isotope data is provided in Supplementary Data 1.

2.3. Garnet Lu–Hf

Garnet Lu–Hf analyses were conducted on a RESOlution 193 nm excimer laser ablation system connected to an Agilent 8900 triple quadrupole (QQQ) ICPMS following the procedures of Simpson et al. (2021). Gas flow parameters for the Laurin Technic S155 laser cell were—Ar carrier gas 0.95 L/min, He Carrier gas 0.32 L/min. The addition of 1.2 ml/min NH_3 (20 % ammonia) in He was used as the reaction gas in the ICPMS, and was tuned to maximise sensitivity for Hf reaction products at +82 added mass (19–20 % of mass flow controller full scale; not calibrated). Laser fluence was 2.7 J/cm^2, with a laser repetition rate of 10 Hz and 130 μm ablation spot size. The following masses were measured sequentially (dwell in ms): ^{27}Al (5), ^{43}Ca (5), ^{47}Ti (5), ^{89}Y (5), ^{90}Zr (5), ^{140}Ce (5), ^{172}Yb (10), $^{172+82}Yb$ (30), ^{175}Lu (10), $^{175+16}Lu$ (20), $^{175+82}Lu$ (100), $^{176+82}Hf$ (100), $^{178+82}Hf$ (100). ^{175}Lu was measured as a proxy for ^{176}Lu, and ^{178}Hf was measured as a proxy for ^{177}Hf. Present day $^{176}Lu/^{175}Lu$ (0.02659) and $^{177}Hf/^{178}Hf$ ratios (0.682) (De Bievre and Taylor, 1993) are assumed. Data were reduced using the Iolite4 software package (Paton et al., 2011), which corrects for background counts, mass bias, and instrument drift. NIST 610 was used as the primary reference material assuming $^{176}Lu/^{177}Hf$ and $^{176}Hf/^{177}Hf$ ratios of 0.1379 ± 0.0005 and 0.282122 ± 0.000009, respectively (Nebel et al., 2009). Our long-term weighted average for $^{176}Lu/^{177}Hf$ and $^{176}Hf/^{177}Hf$ ratios in NIST 612 were 0.1348 ± 0.0004 (n = 6, MSWD = 11.1) and 0.28122 ± 0.00088 (n = 6; MSWD = 5.9), respectively, consistent with their published values (Nebel et al., 2009). To check for systematic errors due to matrix mismatch between the NIST silicate glass and the analysed garnets, we measured an in-house garnet reference from a REE-bearing pegmatite in the Capricorn Orogen, that has been dated by U–Pb zircon at 939 ± 5 Ma (Wingate et al., 2011). The garnet Lu–Hf isochron age for this sample of 923 ± 27 Ma (MSWD = 1.3) is within analytical error of the U–Pb zircon date. Results of Lu–Hf analyses are provided in Supplementary Data 2.

3. Results

3.1. Zircon oxygen isotopes

Oxygen isotope SIMS spot analyses were located in the same textural domain as U–Pb SHRIMP spots following repolishing of the grain mount. Measured zircon δ18O $_{VSMOW}$ values range from 6.7 to 4.5 ‰. Given the metamict nature of core domains and the possibility for secondary alteration, a range of filtering steps permit identification of limits on primary magmatic signatures. Combining U–Pb concordance and $^{16}O^1H/^{16}O$ ratios, the latter measured concurrently with δ18O, has been shown to be effective in distinguishing primary versus altered oxygen isotope values in zircon (Liebmann et al., 2021; Pidgeon et al., 2013; Van Kranendonk et al., 2015). We define $\Delta^{16}O^1H/^{16}O$ as the percentage difference between the median $^{16}O^1H/^{16}O$ in crystalline reference material (91500, PL, and Mud Tank) and analyses of unknowns.

Measured zircon $\Delta^{16}O^1H/^{16}O$ values in Acasta zircon extend from within the range exhibited by crystalline reference zircon to more than 17 times the median value of the reference zircon. We interpret elevated $\Delta^{16}O^1H/^{16}O$ values to indicate H_2O within the zircon structure, likely a function of charge balancing in a metamict structure (Pidgeon et al., 2013). Typical crystalline reference zircon has $\Delta^{16}O^1H/^{16}O$ of ≤10 %. However, OG1, an Archean reference zircon has up to 39 % $\Delta^{16}O^1H/^{16}O$. Considering only analyses within 5 % of concordia, a general secular pattern from values at the extreme heavy end of mantle compositions at 4.0 Ga, to light (sub-mantle) δ18O at >3900 Ma, returning to heavy (supra-mantle) δ18O in the Paleoarchaean is observed, although many of these analyses have $^{16}O^1H/^{16}O$ ratios greater than in crystalline zircon (Fig. 2).

Multiple analyses within the c. 4.0 Ga core of Grain X yield δ18O$_{(VSMOW)}$ values of 5.88 ± 0.15 ‰ (MSWD = 1.2), with $\Delta^{16}O^1H/^{16}O$ implying weak hydration (Fig. 3). Rims and metamict domains within

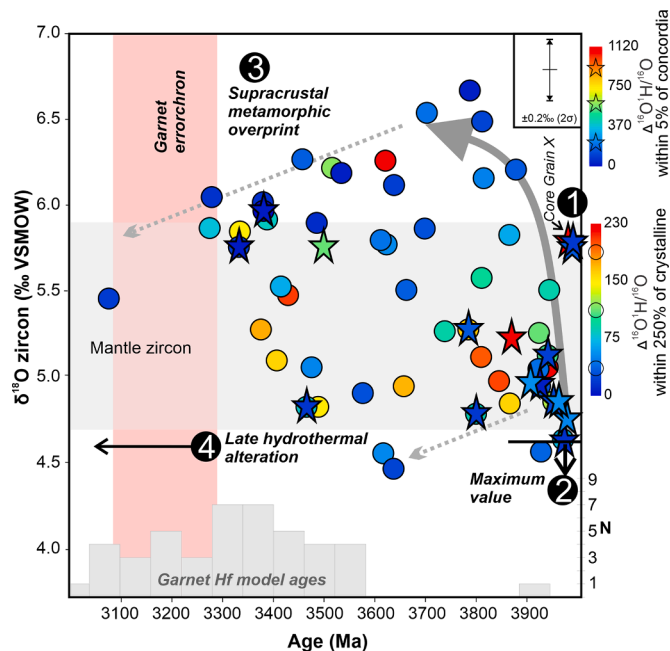**Fig. 2.** Zircon δ18O ‰ versus $^{207}Pb/^{206}Pb$ zircon age evolution plot. The filled circles denote analyses with $\Delta^{16}O^1H/^{16}O$ within 250 % of the crystalline reference zircon. Star symbols denote analyses within 5 % of concordia. Colour scale ramp for each symbol reflects $\Delta^{16}O^1H/^{16}O$. Mantle zircon field of δ18O = 5.3 ± 0.6 ‰. Overlaid histogram is single spot garnet Lu–Hf model ages. The garnet errorchron age is indicated as a pink vertical bar. Stages of zircon evolution as discussed in the text and labelled as white text within black circles. (For interpretation of the references to colour in this figure legend, the reader is referred to the web version of this article.)
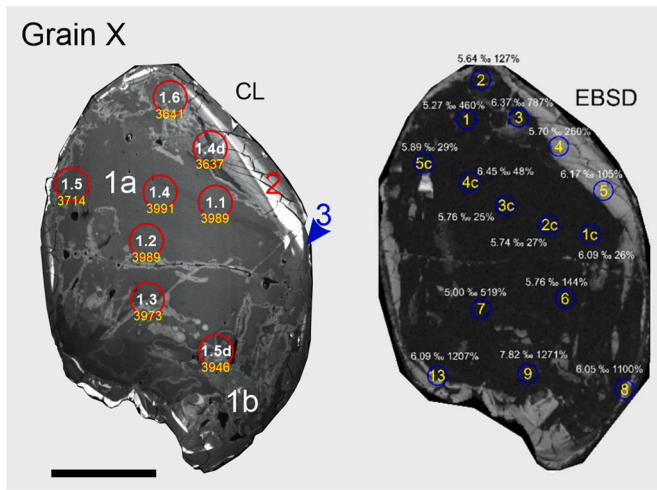
Fig. 3. CL and EBSD images of zircon Grain X. Left = CL image; Right = EBSD band contrast image. The U–Pb zircon analytical spots are shown as red circles, with [207]Pb/[206]Pb ages in yellow font (Ma). Oxygen isotope analytical spots are shown as blue circles, with $\delta^{18}O$ (‰) and relative hydration (%) in white font. Spot IDs are those in data S1. The band contrast image is constructed from all EBSD patterns collected in a given area. Dark regions have poor pattern quality (amorphous), whereas bright regions have good pattern quality (crystalline). Scale bar is 50 μm.(For interpretation of the references to colour in this figure legend, the reader is referred to the web version of this article.)

this ancient grain yield predominantly heavier $\delta^{18}O$ values (of up to 8.6 ‰), but with relatively greater hydration. An analysis on an altered CL bright vein yields a lighter $\delta^{18}O$ value of ~5.0 ‰.

3.2. Garnet Lu–Hf age

Forty-nine LA–ICPMS Lu–Hf analyses of garnet yield an errorchron of 3181 ± 110 Ma, with an initial $^{176}Hf/^{177}Hf$ of 0.250 ± 0.083 (Fig. 4). More radiogenic analyses permit calculation of two-point model ages to assist in understanding isotopic and chemical complexity in this dataset. Pinning the least radiogenic component on an average $^{176}Hf/^{177}Hf$ initial composition of 0.2803 ± 0.0200, which encompasses the entire published range from the Acasta Gneiss, yields model ages that range from 3.9 to 2.8 Ga, with a broad peak between 3.4 and 3.2 Ga. No correlation is apparent between model age and chemistry (Al, Ca, Ti, Y,
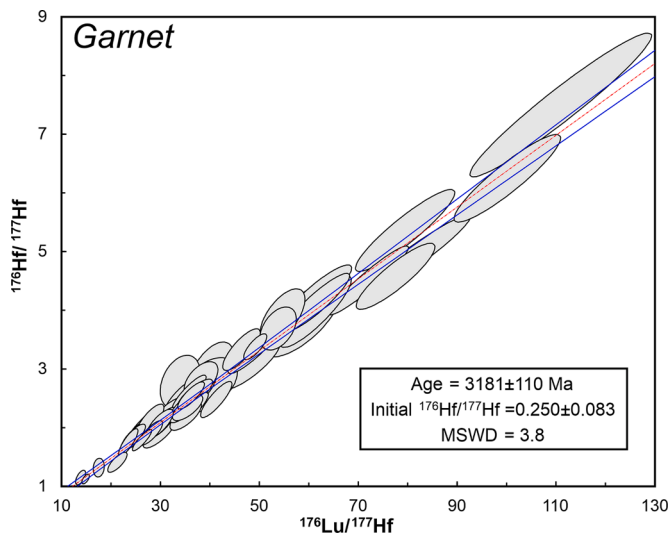

Fig. 4. Garnet Lu–Hf errorchron for sample AC13. Error ellipses are at the 2-sigma level.

Ce, Yb), implying the scatter is not a function of inclusions (Supplementary Fig. S3). We interpret the errorchron to approximate the time of closure to radiogenic Hf in most of these garnet crystals, and to date cooling from a high-grade metamorphic episode at some time between c. 3.3–3.1 Ga. The excess dispersion likely implies domains within garnet became effectively closed to Hf diffusion at different times.

4. Discussion

The garnet Lu–Hf errorchron is consistent with metamorphism and cooling to the effective closure temperature for most of the radiogenic Hf in this mineral between 3.3 to 3.1 Ga (Fig. 4). The closure temperature for garnet Lu–Hf is domain specific and, although affected by several factors (fast diffusion pathways, cooling rate, grain size, etc.), is expected to be at least 600 °C (Simpson et al., 2021). Late Paleoarchean to early Mesoarchean metamorphism and the generation of fluids from prograde metamorphism of supracrustal rocks may have promoted the generation of zircon overgrowths also at this time. Whole rock Lu–Hf geochronology has resolved 3.96 Ga and 3.60 Ga magmatic components in the Acasta gneiss, with some samples recording younger ages and a greater degree of metamorphic overprinting (Guitreau et al., 2014). The complexity of these Lu–Hf dates are consistent with samples yielding 3.37 Ga Sm–Nd isochrons also containing 3.96 Ga magmatic zircon (Mojzsis et al., 2014; Moorbath et al., 1997). Fisher et al. (2020) presented a compilation of bulk rock Sm–Nd isotope data for the Acasta Gneiss, yielding a c. 3.3 Ga errorchron. Although some have argued that a c. 3.3 Ga age may not be geologically meaningful (Bowring and Housh, 1995), more recent U–Pb zircon dating (Bauer et al., 2017) support new growth or modification of zircon at around this time, consistent with the in situ Lu–Hf garnet results from sample AC13.

4.1. Oxygen isotopic signature

The 3.99 Ga oldest core component (Group 1a) is associated with $\delta^{18}O$ of 5.88 ‰ in domains with low $^{16}O^1H/^{16}O$ values that are similar to those within the OG1 reference zircon (Fig. 5). A later phase of
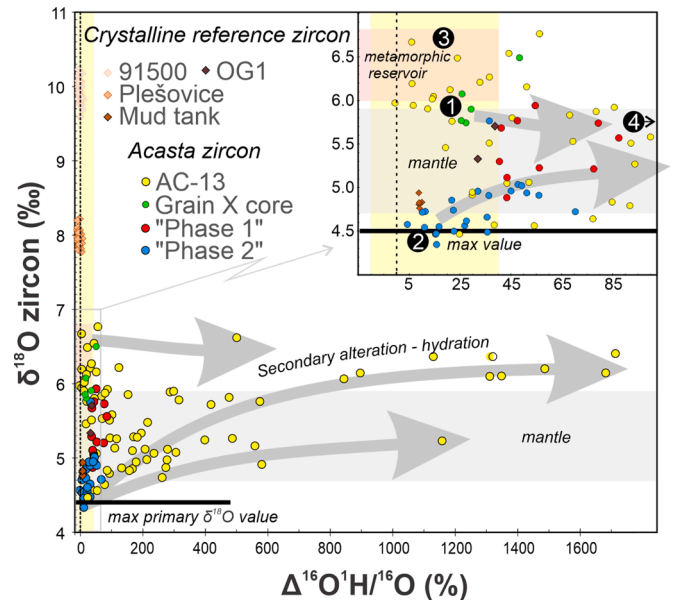

Fig. 5. Relative zircon hydration versus $\delta^{18}O$ (VSMOW). Vertical yellow bar denotes the range of $\Delta^{16}O^1H/^{16}O$ considered to indicate insignificant quantities of H_2O within the zircon structure. Phase I and II zircon from Reimink et al. (2016) has an interpreted primary crystallization age of c. 4.02 Ga. Dashed vertical line is the median relative hydration of crystalline reference zircon.(For interpretation of the references to colour in this figure legend, the reader is referred to the web version of this article.)

concordant zircon has light $\delta^{18}O$ (≤ 4.5 ‰), low $^{16}O^{1}H/^{16}O$ ratios, and an age of at least 3965 Ma (e.g. spot AC-3). Such light oxygen isotopic signatures cannot be the product of sample preparation, as it would require several wt.% H_2O in the zircon structure to deviate $\delta^{18}O$ from primary values (e.g. from 5.3 ‰ to 4.5 ‰), inconsistent with the measured $^{16}O^{1}H/^{16}O$ magnitude in these domains (Supplementary Data S3). Furthermore, a previously analysed set of six Eoarchean–Hadean zircon analyses with low relative hydration have a primary $\delta^{18}O$ of $\leq 4.478 \pm 0.082$ ‰ (MSWD = 0.75) (Reimink et al., 2016).

Younger zircon overgrowths (CL type 3) with an EBSD response suggestive of highly-crystalline zircon have $^{16}O^{1}H/^{16}O$ within the range of reference zircon and $\delta^{18}O \geq 6$ ‰, consistent with growth from fluids and/or melts derived from supracrustal rocks. Elevated $^{16}O^{1}H/^{16}O$ signatures within metamict cores also indicate interaction with supracrustally-derived fluids, involving fractionation between zircon and liquid oxygen isotopes (Valley, 2003). Additionally, oxygen isotope data from zircon fronts (CL type 2) implies that recrystallization at 3520–3380 Ma involved a reservoir with $\delta^{18}O$ above mantle values, consistent with fluids and/or melts liberated during high-grade metamorphism (dehydration and/or melting reactions) and garnet (re)crystallization. Many analyses also imply a later (post-metamorphic) episode of alteration through charge-balance reactions involving interaction between radiation-damaged zircon and meteoric H_2O-rich fluids (De Hoog et al., 2014; Pidgeon et al., 2013, 2017).

In summary, the data suggests at least four major episodes of zircon growth and/or modification (Fig. 2): (1) primary growth in magma with $\delta^{18}O$ at the isotopically-heavy end of mantle values; (2) interaction with magma(s) produced through assimilation and/or partial melting of hydrothermally-altered crust (i.e. fluids with light $\delta^{18}O$); (3) recrystallization, or new growth, of zircon in the presence of isotopically heavy $\delta^{18}O$ metamorphic fluids (≥ 6 ‰); (4) subsequent alteration by meteoric fluids (< 5.3 ‰).

Determining the primary (magmatic) oxygen isotopic signatures for ancient zircon grains from Acasta is difficult given their complex and protracted history. Calculations on the degree of structural modification that these grains should have experienced due to radioactive decay (assuming a lack of annealing), also assessed through EBSD imaging, highlights an important issue in the interpretation of the oxygen isotopic composition of zircon. For example, the study of Reimink et al. (2014) identified several c. 4.02 Ga primary zircon growth components (their 'phase I and II') with $\delta^{18}O$ values that they interpreted to reflect assimilation of low-$\delta^{18}O$ altered crust by the parental magma. Accepting a primary magmatic zircon age of 4.02 Ga, calculations show that average 'phase I' zircon with 442 ppm U and 405 ppm Th would have a density of only 4.2 mg/cc, within the 'highly metamict' stage of Murakami et al. (1991). Nonetheless, our data indicate that such zircon domains may retain primary signatures providing they did not interact with fluid. For example, zircon with 150 ppm U and 89 ppm Th, appropriate for 'phase II', have higher calculated densities (~4.4 mg/cc), with six 'phase II' analyses within the range of crystalline zircon. These 'crystalline' zircon analyses yield $\delta^{18}O$ values between 4.79 and 4.38 ‰, demanding an early light-oxygen source component in the magma from which they crystallised.

Such variable 'phase I and II' zircon oxygen signatures were interpreted to imply shallow-level fractionation of basaltic magma and assimilation of hydrothermally-altered crust (Reimink et al., 2014). Trace element chemistry (no enrichment in LREE) and concordant U–Pb systematics have been argued to suggest a primary zircon component with $\delta^{18}O$ as heavy as 5.9 ‰ in 'phase I' zircon (Reimink et al., 2014, 2020), similar to values seen in the core region of Grain X, from this work (Fig. 3).

A plot of $\Delta^{16}O^{1}H/^{16}O$ versus $\delta^{18}O$ for AGC zircon reveals correlations characteristic of secondary hydration in zircon as well as equilibration with a metamorphic fluid (Fig. 5), for which the least hydrated analyses with $\delta^{18}O$ ~4.5 ‰ is interpreted to provide a maximum limit on a source value for that ≥ 3.97 Ga zircon component. Hence, a bimodal zircon

oxygen isotope signature is apparent in the oldest components of the Idiwhaa gneiss.

4.2. Secular pattern

Craton-scale secular deviations in zircon $\delta^{18}O$ will reflect a combination of local magmatic processes and, potentially, broader planetary geodynamics. At Acasta, the broad secular pattern in zircon oxygen isotopes define bimodal signatures (Fig. 2), including a light component in the Hadean to Paleoarchean, progressing to, on average, heavier signatures in the Mesoarchean. A similar zircon oxygen isotope pattern is also seen in other ancient cratons (Fig. 6). For example, a Pettitt test (Pettitt, 1979) of homogeneity on 3.3–2.6 Ga primary magmatic zircon oxygen values from the Yilgarn Craton highlights a statistically ($p \ll 0.05$) significant temporal variation with a change point at 2670 Ma when $\delta^{18}O$ values rose from 5.3 ‰ to 5.7 ‰. Primary magmatic zircon oxygen values in the Pilbara Craton (Smithies et al., 2021) also show a statistically significant change ($p \ll 0.05$) at 3060 Ma when $\delta^{18}O$ values rose from 5.4 ‰ to 6.5 ‰. Similarly, zircon oxygen isotope data from the Barberton granite–greenstone terrane, South Africa (Wang et al., 2021) reveal a statistically significant change at 3232 Ma when average $\delta^{18}O$ values rose from 5.5 ‰ to 6.4 ‰. In each case, the data show an increase in the proportion of heavy oxygen through time. Although such changes are unlikely to be a function of a single geodynamic process, and occurred over different time periods, the data points towards greater influence of processes favouring light oxygen incorporation into zircon earlier in the evolution of each craton.

Early (≥ 3990 Ma) oxygen isotopic signatures within the Acasta gneiss, which at the upper (heavy) limit of mantle values are consistent with deep melting with or without a minor supracrustal component that underwent low-temperature oxygen exchange with the hydrosphere (e.g. altered greenstones) (Smithies et al., 2021). Importantly, however, *a* ≥ 3965 Ma sub-mantle oxygen signature in zircon requires assimilation or direct melting of altered near-surface crust that had interacted with meteoric water (Taylor, 1971). For example, crustal material with low $\delta^{18}O$ relative to modern upper mantle is relatively uncommon and mostly associated with high-temperature hydrothermal alteration of oceanic crust (ranges mostly from $\delta^{18}O$ of 3 to 9 ‰) or volcanic caldera collapse (Carley et al., 2014; Valley et al., 2005). Iceland, the British Tertiary Province, the Yellowstone volcanic field, and the Bentley Basin in the Musgrave Province are all examples of low $\delta^{18}O$ extensional systems linked with assimilation (with or without partial melting) of hydrothermally-altered supracrustal rocks (Troch et al., 2020).

In most cases, the underlying processes driving the formation of shallow magmatic-to-hydrothermal systems with variable $\delta^{18}O$ are regarded as endogenous, driven by heat derived from within the Earth. These processes generally involve plate-boundary tectonics and/or mantle plumes, which are also the most commonly invoked drivers behind continental crust production on the early Earth (Fischer and Gerya, 2016; Kusky et al., 2018; Rozel et al., 2017). For example, felsic rocks with low $\delta^{18}O$ signatures ('icelandites') formed (and are probably forming) on Iceland, where a mantle plume (providing 'bottom up' heat) impinges on deeply-fractured (and thereby hydrothermally-altered) basaltic rocks of the mid-Atlantic ridge (Halldórsson et al., 2018). Consequently, in terms of geodynamic setting, Iceland has been considered a direct analogy for continental crust formation in the early Earth (Reimink et al., 2014).

By contrast, rather than endogeneous processes, the secular pattern of oxygen isotopes in some ancient cratons has been interpreted as a signature of partial melting of shallow hydrothermally-altered crust induced by meteorite impacts (Johnson et al., 2022; Kirkland et al., 2022) on a cool early Earth (Piani et al., 2020; Valley et al., 2014). Although impact-induced production of crustal nuclei has garnered little support relative to internal mechanisms of crust production (Arndt and Nisbet, 2012; Harrison and Lenardic, 2022; Van Kranendonk, 2010), 'top down' and 'bottom up' models need not operate in isolation
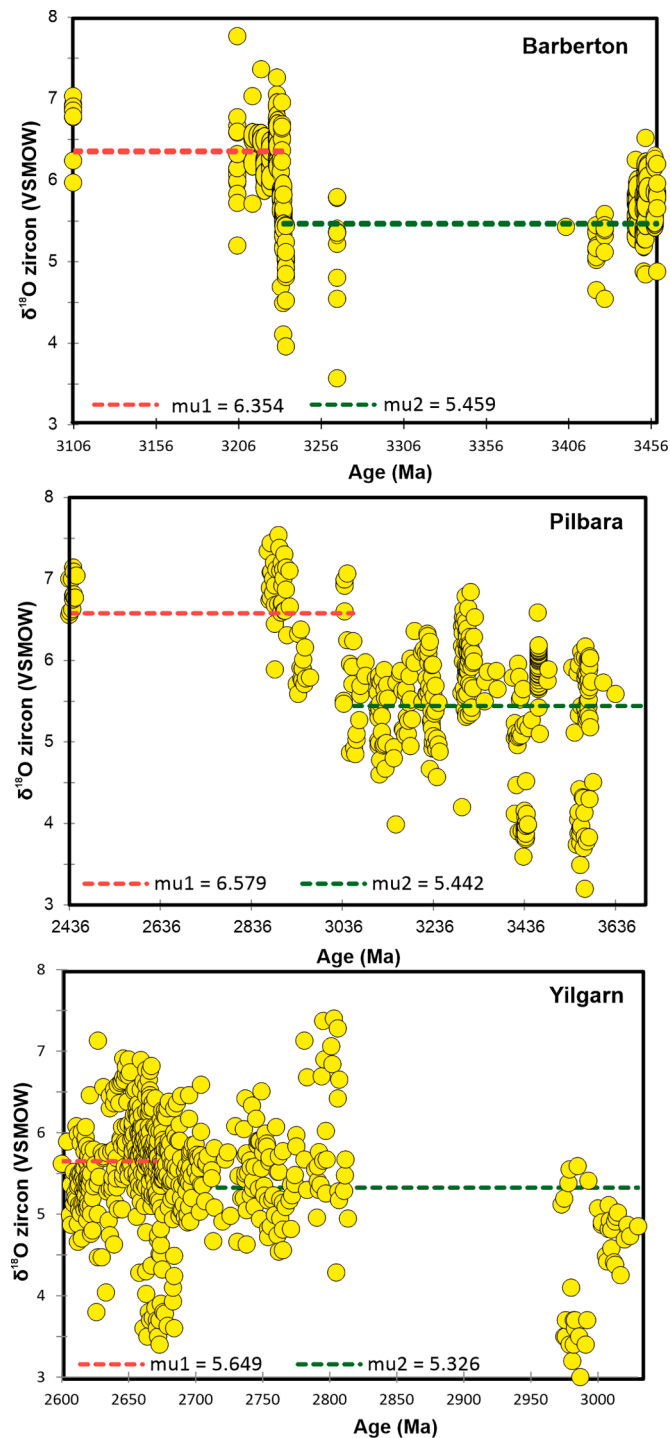
Fig. 6. Zircon oxygen evolution plot for magmatic zircon from various Archean cratons. Pettitt test for homogeneity shown as dashed lines (old green, young red) with average value of δ^{18}O zircon (VSMOW). A broad secular shift to average heavier oxygen is implied. Data from: Yilgarn (Johnson et al., 2022), Pilbara (Smithies et al., 2021), Barberton (Wang et al., 2021). Mu is the statistic representing the population mean of a distribution.(For interpretation of the references to colour in this figure legend, the reader is referred to the web version of this article.)

(O'Neill et al., 2017). Finding a means to distinguish between these two fundamental drivers in the early Earth remains a significant challenge—volcanic caldera and meteorite craters share a great many similarities throughout the rocky planets of our solar system (Slezak et al., 2020; Ubide et al., 2017).

4.3. Endogenic and exogenic drivers

Zircon oxygen isotope time series provide a deep time record of the degree of incorporation into the magma source of material processed at near-surface conditions, and thereby tracks the crustal flux to the deep Earth. At its most simple level, greater heterogeneity in this time series demonstrates a greater range in environmental conditions during magma production. Specifically, lighter δ^{18}O values may be important as they imply interaction with altered supercrustal material (hydrothermally altered by meteoric water at high water/rock ratios in the shallow crust) (Troch et al., 2020) or products of mantle metasomatism (Xu et al., 2021).

The secular pattern of oxygen isotopes in many ancient cratons shows near contemporaneous bimodal signatures with mantle and light values, interpreted by some as a signature of greater influence of impact-derived hydrated crust (Johnson et al., 2022) on a cool early Earth (sometimes) covered with water (Piani et al., 2020; Valley et al., 2014). The global zircon δ^{18}O time series shows greater variance (a measure of how far each measurement in the data set is from the mean) and kurtosis (a measure of the tailedness of the distribution), with a distribution tail towards isotopically lighter values (negative skewness), during proposed times of Milky Way spiral arm transit (Kirkland et al., 2022; Fig. 7). Furthermore, statistical comparison of the zircon δ^{18}O time series kurtosis and a solar system mass density model, using cross correlation analysis (Davis, 1986), reveals a statistically significant positive correlation, which is strongest around the entry point into the spiral arms (Supplementary Data S4; Fig. 7). Such greater tailedness in oxygen isotope distribution, with enhanced isotopically light component, is consistent with a greater proportion of melts produced from assimilation of syn-magmatically altered rocks, around the timing of arm entry.

Specifically, it has been proposed that entry into the galactic spiral arms may have led to gravitational disturbance of the Oort cloud, enhancing the flux of comets towards the inner solar system (Kirkland et al., 2022). This proposition is based on the following points: 1). The prevailing model for our galaxy is a barred four-armed structure that rotates about a central black hole (Vallée, 2013). 2). The density waves that define the arms have an estimated rotation velocity of ~210 km s^{-1} (Camarillo et al., 2018). 3). The solar system is within the co-rotation distance thus a faster estimated rotation of ~240 km s^{-1} (Karachentsev and Makarov, 1996). 4). The implication of this is that the solar system transits the galactic spiral arms, on a best-estimated frequency of approximately 190 Ma^{-1} (Gillman and Erenler, 2019; Kirkland et al., 2022). 5). Interactions with the spiral arms will lead to gravitational effects on the Oort cloud, the reservoir of long period comets (Torres et al., 2019). 6. Comet impacts impart much higher energy than meteorite impacts from the asteroid belt, even though the latter are a greater component of Earth's impact flux (Carry, 2012).

This model for interaction between Earth and its interstellar environment implies periods of enhanced high-energy impact flux, seeding greater heterogeneity in terrestrial zircon oxygen isotope distributions (Johnson et al., 2022; Kirkland et al., 2022). It is also consistent with a higher frequency of lunar impacts through the entry into the Scutum–Centaurus arm, during the putative late heavy bombardment (Fernandes et al., 2013) (Fig. 7).

With only rare exceptions, zircon crystals from mantle-equilibrated magmas exhibit broadly homogenous δ^{18}O values (5.3 ± 0.6 ‰) consistent with a lack of variability in the oxygen isotope compositions of mantle peridotite (Mattey et al., 1994). Small inputs of a near surface component that interacted with liquid water at low temperature into a primitive source magma would measurably raise δ^{18}O from mantle-like values (Garcia et al., 1998). The c. 4.0 Ga oxygen isotopic signature of the Acasta gneiss, at the extreme heavy end of the δ^{18}O range for mantle, may reflect a mantle source component that incorporated material that interacted with water in the surface hydrosphere. What is clearer is that, early in its history, this precursor rock also reacted with a distinctly different component derived from partial melting or assimilation of
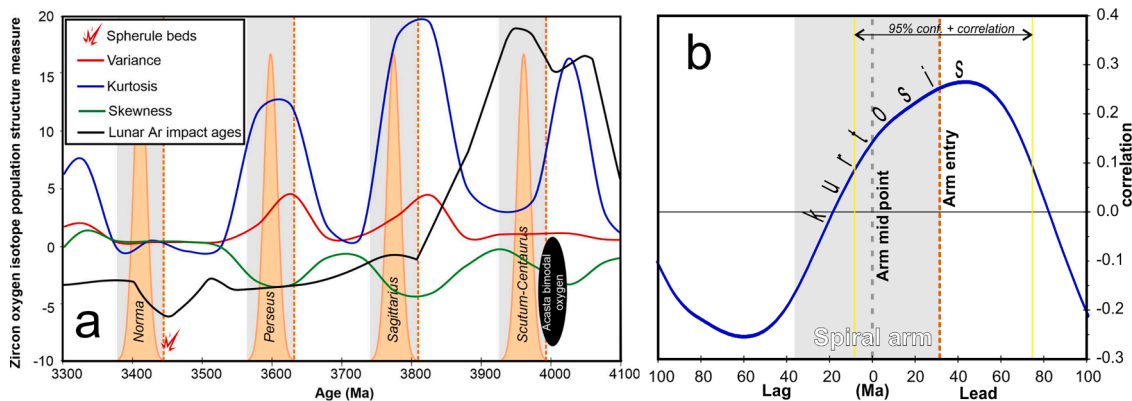
Fig. 7. Population structure of global zircon oxygen isotopes over time. A) Zircon oxygen isotope data from Spencer et al. (2022), on a 50 Ma running temporal bin. Solar system galactic arm transit model (relative mass density) from Kirkland et al. (2022). Spiral arm entry denoted with orange dashed lines. Solid black line indicates cumulative probability curve for lunar ^{40}Ar/^{39}Ar impact glass ages (Fernandes et al., 2013). B) Cross correlation of zircon oxygen time series (kurtosis) versus arm transit model. The correlation temporal scale is centred around the spiral arm mid-point, with entry denoted by a dashed orange line. Spiral arm transit (duration 63 Ma) is denoted by grey fill. Positive correlation at >95 % confidence is indicated between the vertical yellow lines.(For interpretation of the references to colour in this figure legend, the reader is referred to the web version of this article.)

hydrothermally-altered material in the shallow crust. Later metamorphic fluids variably overprinted these primary isotopic signatures.

The favoured model for formation of rocky planets, including Earth, is by collisions (Kokubo and Ida, 2002). Giant impacts are also the preferred explanation for the formation of moons, including Earth's (Ćuk and Stewart, 2012), and recent research has highlighted that erosion from impacting is likely key in explaining the composition of our planet (Frossard et al., 2022). Furthermore, with a significantly higher impact flux than today (Lagain et al., 2022), the early Earth may have developed felsic crustal nuclei through impacting (Dietz, 1964; French, 2004; Glikson, 2007, 2013; Johnson et al., 2022). Primary oxygen isotope signatures from ancient zircon cores in the Idiwhaa gneiss preserve two components—one at the heavy end of mantle values and another isotopically lighter than mantle. The isotopically-light component demands interaction with fluids either directly, or via partial melting, from low-δ^{18}O rocks that themselves had previously undergone high-temperature hydrothermal alteration by surface waters. Globally, a similar secular pattern with oscillations towards negative skewness in zircon oxygen isotopes supports an interpretation of periodic enhanced high-temperature surficial melting. This periodicity in oxygen isotope distribution corresponds to the predicted terrestrial flux of high-energy impactors, based on a Milky Way spiral arm solar system transit model (Kirkland et al., 2022).

5. Conclusions

In early Earth science, it is argued that we should adopt a null hypothesis framed around testing a geodynamic process rooted in plate tectonics (Harrison and Lenardic, 2022). However, planetary accretion can also be advocated as a null hypothesis, with just as robust observational basis grounded in infrared and radio observations of protoplanetary disks around young stars (Kluska et al., 2020) and meteoritics (Maurel et al., 2020), as plate tectonics' plethora of Earth based geophysical and geological evidence. The question then turns to scale and reference frame, Earth based or not, because active processes on our more recent planet may not be a good analogue of the ancient Earth, whereas other rocky bodies in the solar system and elsewhere, just might be. Hence, we favour an important role for impact generation of felsic crustal nuclei on the early Earth (Fig. 8).

Supplementary material

Supplementary Figures S1 to S3 provide additional supporting graphics. Supplementary Data S1 to S2 provides reduced analytical
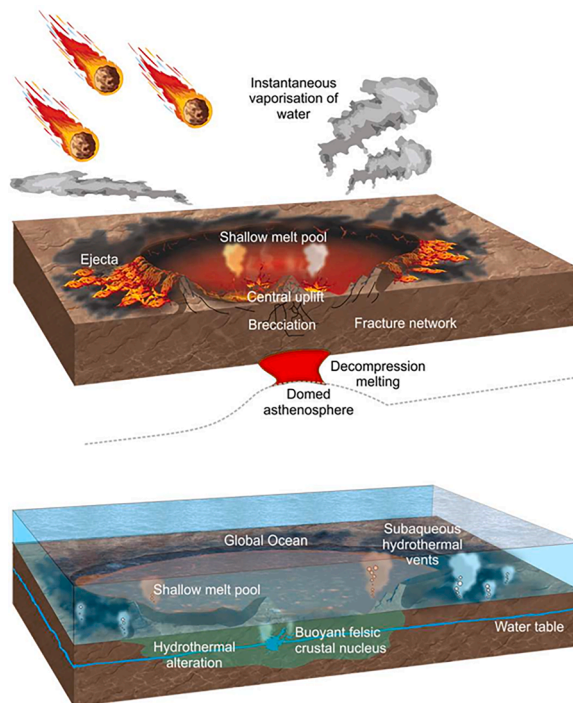

Fig. 8. Schematic cartoon of an impact crater at two stages. Upper; End thermobaric phase with ocean vaporisation and development of a shallow melt pool and deeper decompression mantle melting. Lower; Hydrothermal phase where interaction of near surface processes allows fluid-rock interaction in the brecciated zone and development of light oxygen isotope signatures in zircon crystallizing from the melt pool and during subsequent crustal processing.

datasets in .xlsx format for isotopic analyses. Supplementary Data S3 gives the mixing calculation for zircon—water. Supplementary Data S4 is the cross-correlation analysis.

CRediT authorship contribution statement

C.L. Kirkland: Writing – original draft, Project administration, Formal analysis, Conceptualization. **T.E. Johnson:** Writing – review & editing. **J. Gillespie:** Writing – review & editing, Formal analysis. **L. Martin:** Writing – review & editing, Formal analysis. **K. Rankenburg:**

Writing – review & editing, Formal analysis. **J. Kaempf:** Writing – review & editing, Formal analysis. **C. Clark:** Writing – review & editing.

Declaration of Competing Interest

The authors declare that they have no known competing financial interests or personal relationships that could have appeared to influence the work reported in this paper.

Data availability

All data needed to evaluate the conclusions in the paper are present in the paper and/or the Supplementary Information.

Acknowledgements

Supplementary materials

Supplementary material associated with this article can be found, in the online version, at doi:10.1016/j.epsl.2023.118491.

References

Arndt, N.T., Nisbet, E.G., 2012. Processes on the young Earth and the habitats of early life. Annu. Rev. Earth Planet. Sci. 40, 521–549.

Bauer, A.M., Fisher, C.M., Vervoort, J.D., Bowring, S.A., 2017. Coupled zircon Lu–Hf and U–Pb isotopic analyses of the oldest terrestrial crust, the >4.03 Ga Acasta Gneiss Complex. Earth Planet. Sci. Lett. 458, 37–48.

Bindeman, I., Gurenko, A., Carley, T., Miller, C., Martin, E., Sigmarsson, O., 2012. Silicic magma petrogenesis in Iceland by remelting of hydrothermally altered crust based on oxygen isotope diversity and disequilibria between zircon and magma with implications for MORB. Terra Nova 24, 227–232.

Bowring, S.A., Housh, T., 1995. The Earth's early evolution. Science 269, 1535–1540.

Bowring, S.A., Williams, I.S., 1999. Priscoan (4.00–4.03 Ga) orthogneisses from northwestern Canada. Contrib. Mineral. Petrol. 134, 3–16.

Camarillo, T., Dredger, P., Ratra, B., 2018. Median statistics estimate of the galactic rotational velocity. Astrophys. Space Sci. 363, 268.

Carley, T.L., Miller, C.F., Wooden, J.L., Padilla, A.J., Schmitt, A.K., Economos, R.C., Bindeman, I.N., Jordan, B.T., 2014. Iceland is not a magmatic analog for the Hadean: evidence from the zircon record. Earth Planet. Sci. Lett. 405, 85–97.

Carry, B., 2012. Density of asteroids. Planet. Space Sci. 73, 98–118.

Ćuk, M., Stewart, S.T., 2012. Making the moon from a fast-spinning Earth: a giant impact followed by resonant despinning. Science 338, 1047–1052.

Davis, J.C., 1986. Statistics and Data Analysis in Geology. Wiley.

De Bievre, P., Taylor, P.D.P., 1993. Table of the isotopic compositions of the elements. Int. J. Mass Spectrom. Ion Process. 123, 149–166.

De Hoog, J.C.M., Lissenberg, C.J., Brooker, R.A., Hinton, R., Trail, D., Hellebrand, E., 2014. Hydrogen incorporation and charge balance in natural zircon. Geochim. Cosmochim. Acta 141, 472–486.

Dietz, R.S., 1964. Sudbury structure as an astrobleme. J. Geol. 72, 412–434.

Fernandes, V.A., Fritz, J., Weiss, B.P., Garrick-Bethell, I., Shuster, D.L., 2013. The bombardment history of the Moon as recorded by 40Ar-39Ar chronology. Meteorit. Planet. Sci. 48, 241–269.

Fischer, R., Gerya, T., 2016. Early Earth plume-lid tectonics: a high-resolution 3D numerical modelling approach. J. Geodyn. 100, 198–214.

Fisher, C.M., Bauer, A.M., Vervoort, J.D., 2020. Disturbances in the Sm–Nd isotope system of the Acasta Gneiss Complex—Implications for the Nd isotope record of the early Earth. Earth Planet. Sci. Lett. 530, 115900.

French, B.M., 2004. The importance of being cratered: the new role of meteorite impact as a normal geological process. Meteorit. Planet. Sci. 39, 169–197.

Frossard, P., Israel, C., Bouvier, A., Boyet, M., 2022. Earth's composition was modified by collisional erosion. Science 377, 1529–1532.

Garcia, M.O., Ito, E., Eiler, J.M., Pietruszka, A.J., 1998. Crustal contamination of Kilauea volcano magmas revealed by oxygen isotope analyses of glass and olivine from Puu Oo eruption lavas. J. Petrol. 39, 803–817.

Gillman, M., Erenler, H., 2019. Reconciling the Earth's stratigraphic record with the structure of our galaxy. Geosci. Front. 10, 2147–2151.

Glikson, A., 2007. Chapter 8.5 Early Archean asteroid impacts on Earth: stratigraphic and isotopic age correlations and possible geodynamic consequences (Eds.). In: van Kranendonk, M.J., Smithies, R.H., Bennett, V.C. (Eds.), Developments in Precambrian Geology. Elsevier, pp. 1087–1103.

Glikson, A.Y., 2013. The Asteroid Impact Connection of Planetary Evolution with Special Reference to Large Precambrian and Australian Impacts. Springer Netherlands, Dordrecht.

Guitreau, M., Blichert-Toft, J., Mojzsis, S.J., Roth, A.S.G., Bourdon, B., Cates, N.L., Bleeker, W., 2014. Lu–Hf isotope systematics of the Hadean–Eoarchean Acasta Gneiss Complex (Northwest Territories, Canada). Geochim. Cosmochim. Acta 135, 251–269.

Halldórsson, S.A., Bali, E., Hartley, M.E., Neave, D.A., Peate, D.W., Guðfinnsson, G.H., Bindeman, I., Whitehouse, M.J., Riishuus, M.S., Pedersen, G.B.M., Jakobsson, S., Askew, R., Gallagher, C.R., Guðmundsdóttir, E.R., Gudnason, J., Moreland, W.M., Óskarsson, B.V., Nikkola, P., Reynolds, H.I., Schmith, J., Thordarson, T., 2018. Petrology and geochemistry of the 2014–2015 Holuhraun eruption, central Iceland: compositional and mineralogical characteristics, temporal variability and magma storage. Contrib. Mineral. Petrol. 173, 64.

Harrison, T.M., Lenardic, A., 2022. Burke's law: toward a reasoned discussion of deep time. Elements 18, 354–355.

Johnson, T.E., Gardiner, N.J., Miljković, K., Spencer, C.J., Kirkland, C.L., Bland, P.A., Smithies, H., 2018. An impact melt origin for Earth's oldest known evolved rocks. Nat. Geosci. 11, 795–799.

Johnson, T.E., Kirkland, C.L., Lu, Y., Smithies, R.H., Brown, M., Hartnady, M.I.H., 2022. Giant impacts and the origin and evolution of continents. Nature 608, 330–335.

Karachentsev, I.D., Makarov, D.I., 1996. Orbital velocity of the Sun and the apex of the galactic center. Astron. Lett. 22, 455–458.

Kirkland, C.L., Johnson, T.E., Gillespie, J., Martin, L., 2023. Ion imaging of ancient zircon. Geochem. Perspect. Lett. 27, 38–42.

Kirkland, C.L., Smithies, R.H., Woodhouse, A.J., Howard, H.M., Wingate, M.T.D., Belousova, E.A., Cliff, J.B., Murphy, R.C., Spaggiari, C.V., 2013. Constraints and deception in the isotopic record; the crustal evolution of the west Musgrave Province, central Australia. Gondwana Res. 23, 759–781.

Kirkland, C.L., Sutton, P.J., Erickson, T., Johnson, T.E., Hartnady, M.I.H., Smithies, H., Prause, M., 2022. Did transit through the galactic spiral arms seed crust production on the early Earth? Geology 50, 1312–1317.

Kita, N.T., Ushikubo, T., Fu, B., Valley, J.W., 2009. High precision SIMS oxygen isotope analysis and the effect of sample topography. Chem. Geol. 264, 43–57.

Kluska, J., Berger, J.P., Malbet, F., Lazareff, B., Benisty, M., Le Bouquin, J.B., Absil, O., Baron, F., Delboulbé, A., Duvert, G., Isella, A., Jocou, L., Juhasz, A., Kraus, S., Lachaume, R., Ménard, F., Millan-Gabet, R., Monnier, J.D., Moulin, T., Perraut, K., Rochat, S., Pinte, C., Soulez, F., Tallon, M., Thi, W.F., Thiébaut, E., Traub, W., Zins, G., 2020. A family portrait of disk inner rims around Herbig Ae/Be stars. A&A 636, A116.

Kokubo, E., Ida, S., 2002. Formation of protoplanet systems and diversity of planetary systems. Astrophys. J. 581, 666.

Kusky, T.M., Windley, B.F., Polat, A., 2018. Geological evidence for the operation of plate tectonics throughout the Archean: records from Archean Paleo-plate boundaries. J. Earth Sci. 29, 1291–1303.

Lagain, A., Kreslavsky, M., Baratoux, D., Liu, Y., Devillepoix, H., Bland, P., Benedix, G.K., Doucet, L.S., Servis, K., 2022. Has the impact flux of small and large asteroids varied through time on Mars, the Earth and the Moon? Earth Planet. Sci. Lett. 579, 117361.

Liebmann, J., Spencer, C.J., Kirkland, C.L., Xia, X.-P., Bourdet, J., 2021. Effect of water on δ^{18}O in zircon. Chem. Geol. 574, 120243.

Mattey, D., Lowry, D., Macpherson, C., 1994. Oxygen isotope composition of mantle peridotite. Earth Planet. Sci. Lett. 128, 231–241.

Maurel, C., Bryson, J.F.J., Lyons, R.J., Ball, M.R., Chopdekar, R.V., Scholl, A., Ciesla, F.J., Bottke, W.F., Weiss, B.P., 2020. Meteorite evidence for partial differentiation and protracted accretion of planetesimals. Sci. Adv. 6, eaba1303.

Mojzsis, S.J., Cates, N.L., Caro, G., Trail, D., Abramov, O., Guitreau, M., Blichert-Toft, J., Hopkins, M.D., Bleeker, W., 2014. Component geochronology in the polyphase ca. 3920 Ma Acasta gneiss. Geochim. Cosmochim. Acta 133, 68–96.

Moorbath, S., Whitehouse, M.J., Kamber, B.S., 1997. Extreme Nd-isotope heterogeneity in the early Archaean—Fact or fiction? Case histories from northern Canada and West Greenland. Chem. Geol. 135, 213–231.

Murakami, T., Chakoumakos, B.C., Ewing, R.C., Lumpkin, G.R., Weber, W.J., 1991. Alpha-decay event damage in zircon. Am. Mineral. 76, 1510–1532.

Nebel, O., Morel, M., Vroon, P., 2009. Isotope dilution determinations of Lu, Hf, Zr, Ta and W and Hf isotope compositions of NIST SRM 610 and 612 glass wafers. Geostand. Geoanal. Res. 33, 487–499.

O'Neil, J.R., Chappell, B.W., 1977. Oxygen and hydrogen isotope relations in the Berridale batholith. J. Geol. Soc. Lond. 133, 559.

O'Neill, C., Marchi, S., Zhang, S., Bottke, W., 2017. Impact-driven subduction on the Hadean Earth. Nat. Geosci. 10, 793–797.

Paton, C., Hellstrom, J., Paul, B., Woodhead, J., Hergt, J., 2011. Iolite: freeware for the visualisation and processing of mass spectrometric data. J. Anal. At. Spectrom. 26, 2508–2518.

Pettitt, A.N., 1979. A non-parametric approach to the change point problem. J. R. Stat. Soc. Ser. C Appl. Stat. 28, 126–135.

Piani, L., Marrocchi, Y., Rigaudier, T., Vacher Lionel, G., Thomassin, D., Marty, B., 2020. Earth's water may have been inherited from material similar to enstatite chondrite meteorites. Science 369, 1110–1113.

Pidgeon, R.T., Nemchin, A.A., Cliff, J., 2013. Interaction of weathering solutions with oxygen and U–Pb isotopic systems of radiation-damaged zircon from an Archean granite, Darling Range Batholith, Western Australia. Contrib. Mineral. Petrol. 166, 511–523.

Pidgeon, R.T., Nemchin, A.A., Whitehouse, M.J., 2017. The effect of weathering on U–Th–Pb and oxygen isotope systems of ancient zircons from the Jack Hills, Western Australia. Geochim. Cosmochim. Acta 197, 142–166.

Reimink, J.R., Chacko, T., Stern, R.A., Heaman, L.M., 2014. Earth's earliest evolved crust generated in an Iceland-like setting. Nat. Geosci. 7, 529–533.

Reimink, J.R., Chacko, T., Stern, R.A., Heaman, L.M., 2016. The birth of a cratonic nucleus: lithogeochemical evolution of the 4.02–2.94 Ga Acasta Gneiss Complex. Precambrian Res. 281, 453–472.

Reimink, J.R., Davies, J.H.F.L., Bauer, A.M., Chacko, T., 2020. A comparison between zircons from the Acasta Gneiss Complex and the Jack Hills region. Earth Planet. Sci. Lett. 531, 115975.

Rozel, A.B., Golabek, G.J., Jain, C., Tackley, P.J., Gerya, T., 2017. Continental crust formation on early Earth controlled by intrusive magmatism. Nature 545, 332–335.

Simpson, A., Gilbert, S., Tamblyn, R., Hand, M., Spandler, C., Gillespie, J., Nixon, A., Glorie, S., 2021. In-situ Lu single bond Hf geochronology of garnet, apatite and xenotime by LA ICP MS/MS. Chem. Geol. 577, 120299.

Slezak, T.J., Radebaugh, J., Christiansen, E.H., Belk, M.C., 2020. Classification of planetary craters using outline-based morphometrics. J. Volcanol. Geotherm. Res. 407, 107102.

Smithies, R.H., Kirkland, C.L., Cliff, J.B., Howard, H.M., Quentin de Gromard, R., 2015. Syn-volcanic cannibalisation of juvenile felsic crust: superimposed giant ^{18}O-depleted rhyolite systems in the hot and thinned crust of Mesoproterozoic central Australia. Earth Planet. Sci. Lett. 424, 15–25.

Smithies, R.H., Lu, Y., Kirkland, C.L., Johnson, T.E., Mole, D.R., Champion, D.C., Martin, L., Jeon, H., Wingate, M.T.D., Johnson, S.P., 2021. Oxygen isotopes trace the origins of Earth's earliest continental crust. Nature 592, 70–75.

Spencer, C.J., Cavosie, A.J., Morrell, T.R., Lu, G.M., Liebmann, J., Roberts, N.M.W., 2022. Disparities in oxygen isotopes of detrital and igneous zircon identify erosional bias in crustal rock record. Earth Planet. Sci. Lett. 577, 117248.

Stern, R.A., Bleeker, W., 1998. Age of the world's oldest rocks refined using Canada's SHRIMP: the Acasta Gneiss Complex, Northwest Territories, Canada. Geosci. Canada 25, 27–31.

Taylor, H.P., 1971. Oxygen isotope evidence for large-scale interaction between meteoric ground waters and Tertiary Granodiorite Intrusions, Western Cascade Range, Oregon. J. Geophys. Res. (1896–1977) 76, 7855–7874.

Torres, S., Cai, M.X., Brown, A.G.A., Zwart, S.P., 2019. Galactic tide and local stellar perturbations on the Oort cloud: creation of interstellar comets. A&A 629, A139.

Troch, J., Ellis, B.S., Harris, C., Bachmann, O., Bindeman, I.N., 2020. Low-δ^{18}O silicic magmas on Earth: a review. Earth-Science Rev. 208, 103299.

Ubide, T., Guyett, P.C., Kenny, G.G., O'Sullivan, E.M., Ames, D.E., Petrus, J.A., Riggs, N., Kamber, B.S., 2017. Protracted volcanism after large impacts: evidence from the Sudbury impact basin. J. Geophys. Res. 122, 701–728.

Vallée, J.P., 2013. A synthesis of fundamental parameters of spiral arms, based on recent observations in the Milky Way. Int. J. Astron. Astrophys. 03 (01), 9.

Valley, J.W., 2003. Oxygen isotopes in zircon. Rev. Mineral. Geochem. 53, 343–385.

Valley, J.W., Cavosie, A.J., Ushikubo, T., Reinhard, D.A., Lawrence, D.F., Larson, D.J., Clifton, P.H., Kelly, T.F., Wilde, S.A., Moser, D.E., Spicuzza, M.J., 2014. Hadean age for a post-magma-ocean zircon confirmed by atom-probe tomography. Nat. Geosci. 7, 219–223.

Valley, J.W., Lackey, J.S., Cavosie, A.J., Clechenko, C.C., Spicuzza, M.J., Basei, M.A.S., Bindeman, I.N., Ferreira, V.P., Sial, A.N., King, E.M., Peck, W.H., Sinha, A.K., Wei, C. S., 2005. 4.4 billion years of crustal maturation: oxygen isotope ratios of magmatic zircon. Contrib. Mineral. Petrol. 150, 561–580.

Van Kranendonk, M.J., 2010. Two types of Archean continental crust: plume and plate tectonics on early Earth. Am. J. Sci. 310, 1187.

Van Kranendonk, M.J., Kirkland, C.L., Cliff, J., 2015. Oxygen isotopes in Pilbara Craton zircons support a global increase in crustal recycling at 3.2 Ga. Lithos 228–229, 90–98.

Wang, X., Tang, M., Moyen, J., Wang, D., Kröner, A., Hawkesworth, C., Xia, X., Xie, H., Anhaeusser, C., Hofmann, A., Li, J., Li, L., 2021. The onset of deep recycling of supracrustal materials at the Paleo-Mesoarchean boundary. Natl. Sci. Rev. nwab136.

Wiedenbeck, M., AllÉ, P., Corfu, F., Griffin, W.L., Meier, M., Oberli, F., Quadt, A.V., Roddick, J.C., Spiegel, W., 1995. Three natural zircon standards for U–Th–Pb, Lu–Hf, trace element and REE analysis. Geostand. Newsl. 19, 1–23.

Wingate, M.T.D., Kirkland, C.L., Johnson, S.P., 2011. 190667: granite pegmatite, Camel Hill. In: Geological Survey of Western Australia Geochronology Record, 6.

Xu, J.-Y., Giuliani, A., Li, Q.-L., Lu, K., Melgarejo, J.C., Griffin, W.L., 2021. Light oxygen isotopes in mantle-derived magmas reflect assimilation of sub-continental lithospheric mantle material. Nat. Commun. 12, 6295.